Probing Hundreds of Individual Quantum Defects in Polycrystalline and Amorphous Alumina

Chih-Chiao Hung,[1,2,3] Liuqi Yu[1,2] Neda Foroozani,[1,2] Stefan Fritz,[4] Dagmar Gerthsen,[4] and Kevin D. Osborn[1,2,5,*]

[1]*Laboratory for Physical Sciences, 8050 Greenmead Drive, College Park, Maryland 20740, USA*
[2]*Quantum Materials Center, University of Maryland, College Park, Maryland 20742, USA*
[3]*Department of Physics, University of Maryland, College Park, Maryland 20742, USA*
[4]*Laboratory for Electron Microscopy, Karlsruhe Institute of Technology, 76131 Karlsruhe, Germany*
[5]*Joint Quantum Institute, University of Maryland, College Park, Maryland 20742, USA*

Quantum two-level systems (TLSs) are present in the materials of qubits and are considered defects because they limit qubit coherence. For superconducting qubits, the quintessential Josephson junction barrier is made of amorphous alumina, which hosts TLSs. However, TLSs are not generally understood, either structurally or in atomic composition. In this study, we greatly extend the quantitative data available on TLSs by reporting on the physical dipole moment in two alumina types: polycrystalline γ-Al$_2$O$_3$ and amorphous a-AlO$_x$. To obtain the dipole moments p_z, rather than the less-structural coupling parameter g, we tune individual TLSs with a known external electric field in a cavity quantum electrodynamic system. We find a clear difference in the dipole moment distribution from the film types, indicating a difference in TLS structures. A large sample of approximately 400 individual TLSs are analyzed from the polycrystalline film type. Their dipoles along the growth direction p_z have a mean value of 2.6 ± 0.3 debye (D) $(0.54 \pm 0.06 \, e\,\text{Å})$ and standard deviation $\sigma = 1.6 \pm 0.2$ D $(0.33 \pm 0.03 \, e\,\text{Å})$. The material distribution fits well to a single Gaussian function. Approximately 200 individual TLSs are analyzed from amorphous films. Both the mean $p_z = 4.6 \pm 0.5$ D $(0.96 \pm 0.1 \, e\,\text{Å})$ and $\sigma = 2.5 \pm 0.3$ D $(0.52 \pm 0.05 \, e\,\text{Å})$ are larger. Amorphous alumina also has very large p_z, greater than 8.6 D $(1.8 \, e\,\text{Å})$, in contrast to polycrystalline which has none of this moment. These large moments agree only with oxygen-based TLS models. Based on data and the candidate models (delocalized O and hydrogen-based TLSs), we find polycrystalline alumina has smaller ratio of O-based to H-based TLS than amorphous alumina.

I. INTRODUCTION

Long coherence times are essential for quantum information processing, and this implies high-quality Josephson junctions (JJs) in superconducting qubits [1–6]. For over a dozen years, quantum tunneling two-level systems (TLSs) have been known to be defects that cause loss and limit coherence of qubits [7,8]. In addition, TLSs create telegraphic noise and $1/f$ - noise [9–11] in superconducting qubits [12–14], semiconducting qubits [15], and astronomy photon detectors [16,17]. There are several strategies to improve the qubit coherence time such as material optimization [18–21], surface treatments [21–23], and engineering of the qubit geometry to decrease the participation of TLSs [24–26].

In the quintessential JJ, an amorphous alumina barrier is grown thermally on the surface of aluminum [1,2,4]. Loss tangents of amorphous alumina in JJs [18] and in grown films [27] are measured to be approximately 2×10^{-3}, much higher than that in crystalline alumina from the sapphire substrates used for qubit fabrication [28]. Accordingly, amorphous materials are believed to have higher loss than crystalline ones due to additional tunneling degrees of freedom (TLSs) in the former. Hexagonal boron nitride and other two-dimensional materials are being investigated for JJs [29–31], but an alternative method to improve the JJ barrier uses annealed crystalline alumina [32,33]. Crystalline alumina studies show a decrease in both TLS density [32] and TLS–qubit couplings, g, relative to amorphous alumina [33].

*kosborn@umd.edu

Recent TLS analysis techniques use dc-tuned electric [34–37] or strain fields [38–40] for the observation of individual nanoscale defects. According to the Standard Tunneling Model [41,42], individual TLSs have a dipole moment p, transition energy E, and tunneling energy Δ_0. Generally, the TLS is described as tunneling charge presumed to be an atom or small group of atoms, though a recent study reports on a possibility of trapped quasiparticles [43]. Their identification is a 50-year-old mystery [44].

TLSs have an ac coupling to quantum systems,

$$g = \frac{\Delta_0}{E} \frac{2 \, p_z E_{\mathrm{rms}}}{\hbar},\tag{1}$$

which is related to dipole moment component p_z along zero-point fluctuation of electric field $\mathbf{E}_{\mathrm{rms}}$. However, the most common measurement of g does not allow extraction of p_z because Δ_0 is unknown or E_{rms} is not uniform [8,32,33]. On the other hand, uniform dc-biased measurements allow measurements of individual p_z [34,35] and dynamically biased experiments extract averaged p_z [45]. Such dynamical bias can induce Landau-Zener transitions, and recent work shows that a resonator can even exhibit dynamical decoupling using these transitions [46]. Recently, voltage bias gates have been added above or below the target area to tune TLSs [36,37]. The extraction of dipoles is possible from g and the extracted position, but the distribution is given as a function of g rather than p_z [36]. Also, only small samples of p_z were directly extracted in the past: 13 in amorphous alumina [35] and 64 in silicon nitride [34]. A comparison of p_z in two different materials has not been performed in a single study.

In this paper we study individual TLSs in both polycrystalline alumina γ-Al$_2$O$_3$ and amorphous alumina a-AlO$_x$. We follow the circuit schematic of Ref. [34], which we call an electrical-bridge quantum-defect sensor. The TLSs were analyzed in films with an approximate thickness of 20 nm. The TLSs in γ-Al$_2$O$_3$ films are relatively stable, and allow us to obtain a large distribution of 394 TLS dipole moments p_z. In a-AlO$_x$ films, 189 TLS moments are extracted despite higher TLS noise. Compared to the γ-Al$_2$O$_3$ film, larger averaged dipole and standard deviation σ are extracted in a-AlO$_x$ films and 10% of TLSs have larger dipole than the maximum extracted in γ-Al$_2$O$_3$. Specific TLS structures were proposed using available information from recent work on density functional theory (DFT) analysis of TLSs in alumina, where both hydrogen [47,48] and oxygen [49–51] based TLS have been proposed as the interstitial defects. A comparison of the dipole moments for both γ-Al$_2$O$_3$ and a-AlO$_x$ film types allows possible TLS origin identification.

II. METHOD

Fabrication starts by *in situ* growth of Al/alumina/Al trilayers on a 3-inch Si substrate, where the alumina is the material hosting the TLSs. The *in situ* method prevents substantial hydrogen contamination, but diffusion of hydrogen is also difficult to prevent in standard lithographic processing [52]. Then a first BCl$_3$ etch forms a mesa into the top two layers, defining four equal capacitors ($C_1, \ldots, C_4$). Next, a second BCl$_3$ etch forms the base metal including a resonator inductor L and a ground plane. Finally, silicon nitride is deposited as a wiring dielectric, vias are etched by SF$_6$, and an Al wiring layer is defined to connect the inductor to the capacitors. This creates the final resonator structure as shown in Fig. 1(a). Alumina in the dielectric layer is designed to have an approximate
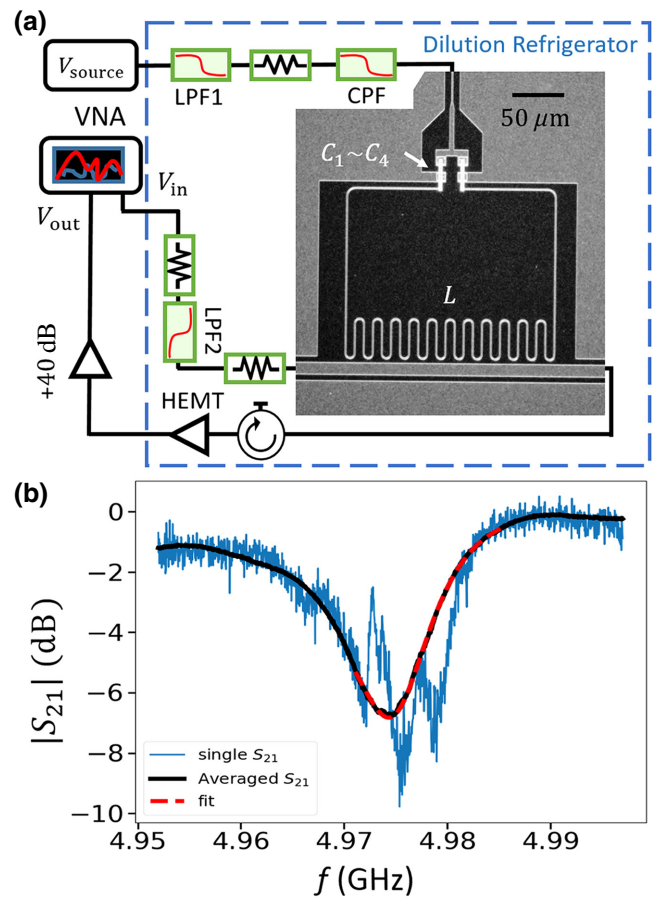

FIG. 1. (a) Optical image of microwave resonator with an abbreviated wiring schematic. The source voltage is filtered through an *RC* low-pass filter and a copper powder filter (CPF). The combination of resistance in the *RC* filter and the 3 dB attenuator gives $V_{\mathrm{bias}} = 9.56 \times 10^{-3} \times V_{\mathrm{source}}$. (b) $|S_{21}|$ of one γ-Al$_2$O$_3$ resonator. It shows multiple dips indicating TLSs strongly coupled to the resonator. The black curve is the ensemble average $|S_{21,\mathrm{avg}}|$, obtained by averaging S_{21} from different bias voltages. The intrinsic quality Q_i is $1/(1.47 \times 10^{-3}) \approx 680$ according to the red fitted line.

thickness $d = 20$ nm and a volume $\mathbb{V} = 1.11 \times 10^{-17}$ m^3 in each capacitor.

The two sample types are grown in separate chambers. The polycrystalline sample has a 20-nm-thick γ-Al$_2$O$_3$ film deposited by electron-beam evaporation from 99.99% purity Al$_2$O$_3$ pellets with a base pressure of less than 5×10^{-7} torr, and alumina is sandwiched by two 100-nm-thick aluminum films. On the other hand, the a-AlO$_x$ film is 14.7 nm thick with $x = 1.3 \pm 0.1$ and is grown by iterating eight rounds of 1 nm Al deposition followed by static oxidation at 9.5 mbar of oxygen at 250 °C as described in Ref. [53]. Given this oxidation condition, no long-range ordered (crystalline) structure was detected from transmission electron microscopy and only 3% unoxidized aluminum was found inside the a-AlO$_x$ layer. Transmission electron microscopy shows that the thickness can vary from 10 to 20 nm in some rare cases.

The resonator inductively couples to the transmission line so that a two-port microwave transmission measurement can be carried out. The applied voltage from room temperature is filtered by an RC filter, 3 dB attenuator and a copper powder filter. It generates a dc-biased field E_{ex} across each capacitor. The maximum E_{ex} is 90 kV/m with which we observe no refrigerator heating, thus no significant leakage current. Two resonators were fabricated per chip with nominally the same capacitors, but with different value inductors, giving resonance frequencies of approximately $f_0 = 5.0$ GHz and 4.4 GHz. The resonators were measured at or below 60 mK. A probing photon number $\bar{n} < 1$ is used for all the reported data, to allow observation of TLSs near their ground state.

With a known external field E_{ex}, the asymmetry energy Δ is shifted as $\Delta' = \Delta + 2p_z E_{\text{ex}}$ [34]. Therefore, the resultant TLS energy is

$$E = \sqrt{(\Delta + 2p_z E_{\text{ex}})^2 + \Delta_0^2}. \qquad (2)$$

The resonator constitutes a circuit quantum electrodynamic system with a Jaynes-Cummings model modified for many TLSs. TLSs can be resolved individually by the resonator when the cooperativity $g^2/\gamma_{\text{TLS}}\kappa \geq 1$ [54], where γ_{TLS} is the TLS decay rate for the strongly coupled TLS, and $\kappa = \kappa_e + \kappa_i$ is the resonator decay rate from external coupling and internal loss. We increase the g and cooperativity by reducing $\mathbb{V}$, since $E_{\text{rms}} = \sqrt{hf_0/8\epsilon_r\epsilon_0\mathbb{V}}$ in our parallel-plate capacitor resonator [8].

A single transmission trace $|S_{21}|$ is shown in Fig. 1(b) from a γ-Al$_2$O$_3$ resonator. Within the bandwidth of the resonator, a few fine resonance dips reveal the energies of individual TLSs. However, the TLSs often only couple weakly to the resonator. Therefore, we obtain an approximate intrinsic material loss tangent $\tan\delta_0$ by using the averaged S_{21} traces from different voltage biases, yielding an ensemble-averaged $S_{21,\text{avg}}$. The $|S_{21,\text{avg}}|$ component of

the result is shown as the solid black curve in Fig. 1(b). A fit (dashed red curve) to $S_{21,\text{avg}}$ yields $\tan\delta_0 = 1/Q_i = 1/680 = 1.5 \times 10^{-3}$ and the external (or coupling) quality factor is extracted as $Q_e = 2\pi f_0/\kappa_e = 590$. The same procedure performed on a-AlO$_x$ gives an intrinsic loss tangent of $\tan\delta_0 = 1/\overline{Q_i} = 1/1020 = 9.8 \times 10^{-4}$, which is smaller than that of γ-Al$_2$O$_3$. $\overline{Q_i}$ is the averaged Q_i of a-AlO$_x$ and its Q_i are distinct with every cooldown, unlike γ-Al$_2$O$_3$ (Appendix C). Our loss tangents are similar to alumina with different growth methods, where the loss is measured at $\tan\delta_0 = 1.6 \times 10^{-3}$ [8,55], 7×10^{-4} [56], and 1.6×10^{-3} [57]. Below we discuss TLSs measured in both alumina film types using two resonators for each type.

III. RESULTS AND DISCUSSION

Figure 2(a) shows a TLS spectrum example, $|S_{21}|$, as a function of frequency f and the dc field E_{ex} for γ-Al$_2$O$_3$ measured on one of the two resonators during one cooldown. TLS energies exhibit hyperbolic energies versus E_{ex}, as shown in Fig. 2(a) in agreement with Eq. (2). Similar spectra have been observed and analyzed in a previous study on silicon nitride [34]. One can estimate Δ_0 from the minimum of the TLS energy ($hf_m = \Delta_0$), and p_z from the hyperbola—a steeper curvature gives a larger dipole moment. A optimized Monte Carlo fit is performed on each TLS energy to extract p_z of the specific TLS (see Appendix D). Only well-defined TLS energy curves are selected for analysis. Example fits are plotted as blue hyperbolas in Fig. 2(b).

TLSs change their energies randomly during cooldowns from room temperature. From four different cooldowns, we created different sets of TLSs in the two resonators with one material type. According to the standard TLS distribution [41], TLSs have log-uniform tunneling energies such that there are negligible distribution changes for TLS tunneling energies that are only 0.6 GHz different in our two resonator frequencies (see Appendix E). We therefore combine all the data from different runs in the two resonators to enlarge the sampling number and improve the statistics: a total of 394 TLSs from two resonators are analyzed to form the measured p_z distribution $H(p_z)$ with an average of 3.5 ± 0.4 debye (D) shown in Fig. 2(c). The accuracy of extraction is limited by the uniformity of thickness of alumina rather than the fitting process. Large amounts of individual TLSs allow relatively accurate representation of the TLS moments in γ-Al$_2$O$_3$.

Though the measured polycrystalline distribution $H(p_z)$ has a mean value of 3.5 D, this is not an intrinsic material property. At a given electric field bias range ΔE_{ex}, TLSs with larger dipole moments have a larger shift in asymmetry energy Δ' relative to smaller moments, and this leads to a higher probability of the former moments having
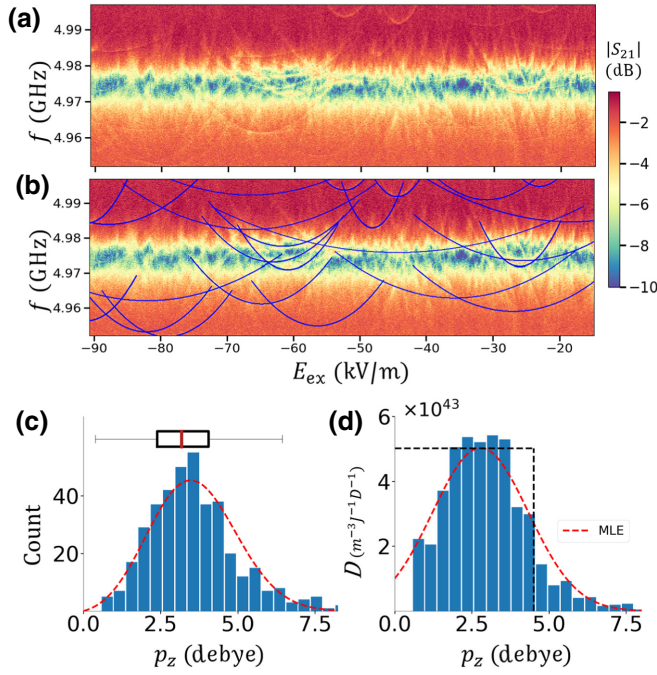
FIG. 2. Data on nanoscale thick γ-Al$_2$O$_3$(polycrystalline) film in circuit quantum electrodynamic system. (a) Color scale plot of transmission $|S_{21}|$ versus frequency f and electric field E_{ex}. Data show a main resonance at 4.974 GHz. Several local minima in $|S_{21}|$ reveal the energy of individual TLSs. (b) Several TLSs in blue hyperbolas are fitted to the energy model [Eq. (2)], where p_z comes from the curvature of the energy hyperbola. (c) The entire data set from this film type yields 394 moments p_z. The red dashed line is a Gaussian function multiplied by p_z as fitted to data. A Seaborn box is plotted, where the red color line is the mean line and the right and left side of box represent the 25th and 75th percentiles of dipole data. (d) Material TLS density of p_z after accounting for the experimental weighing factor. A red dashed Gaussian line is shown with the corresponding fit parameters in (c). From the fit we report the material mean p_z of 2.6 D and standard deviation $\sigma = 1.6$ D. The black dashed line illustrates a possible material density if we assume an isotropic TLS direction.

their energy minimum within the resonator bandwidth (see Appendix A and Ref. [34]). The intrinsic material TLS dipole distribution $D(p_z)$ is related to TLS material density $P_0 = \int D(p_z) \, dp_z$ (in units of $J^{-1}m^{-3}$), and can be calculated from $D(p_z) = \frac{1}{\mathbb{V}} \frac{H(p_z)}{2p_z} \frac{1}{\Delta E_{ex}} \frac{f_0}{\Delta f_0}$, where f_0 is the resonator frequency and Δf_0 is the frequency span of the S_{21} measurement. The red dashed line in Fig. 2(c) shows a fit using a maximum likelihood estimation (MLE) method. The fitting function is a modified Gaussian distribution, which is a Gaussian distribution multiplied by p_z. The TLS material density $D(p_z)$ is shown in Fig. 2(d), where the red line shows a Gaussian function matching the fit parameters in Fig. 2(c).

From the fit, we find that the polycrystalline material distribution $D(p_z)$ has a fitted mean dipole moment of

$\bar{p}_z = 2.6 \pm 0.3$ D ($= 0.54 \pm 0.05 \, e$ Å) and $\sigma = 1.6$ D ($= 0.33 \, e$ Å). The computed TLS density P_0 is $1.0 \pm 0.1 \times 10^{44}$ ($J^{-1}m^{-3}$). This computed value of TLS density along with the dipole moments agrees with the measured loss tangent. As a result we used the material units in Fig. 2(d) for the distribution $D(p_z)$.

For amorphous samples or random voids within polycrystals, we expect TLS dipoles to be random in angle (isotropic). For the case of one single dipole magnitude p_0 and uniform distribution in $\cos\theta$, where θ is the angle of dipole to the z axis, isotropy results. Therefore, $D(p_z)$ is expected to be independent of p_z until the maximum value p_0. As a guide to the eye, an isotropic distribution (random angle) with dipole moment $p_0 = 4.5$ D is shown as a black dashed line in Fig. 2(d). The positive slope in the observed distribution indicates that we have a departure from isotropic distribution (isotropic TLSs give only oppositive slope). Thus, data in Fig. 2(d) show that γ-Al$_2$O$_3$ TLSs can be different than the standard model for TLSs (designated for amorphous samples [41,42]). The anisotropic angular distribution may be caused by the polycrystalline film texture (crystallite orientation) which influences the TLS orientation.

Figure 3(a) shows transmission spectroscopy results for a-AlO$_x$. However, the a-AlO$_x$ spectra are not as clear those of γ-Al$_2$O$_3$ due to higher noise in the spectra, despite using the same setup. To improve the TLS signal contrast, the transmission (S_{21}) data are shown after processing, unlike the polycrystalline film data shown earlier. For our first processing step we chose to subtract $S_{21,avg}$ from S_{21}, and further increase contrast using the formula $[S_{21}(dB) - S_{21,avg}(dB)] \times |S_{21,avg}|$. As a second and third processing step, we apply a low-pass filter in the frequency direction and then take the derivative with respect to frequency. The final result is plotted in arbitrary units in Figs. 3(a) and 3(b), where we added hyperbolic fitting lines (blue lines) to the panel (b).

As we will show in detail below, TLSs within a-AlO$_x$ are less stable than those in γ-Al$_2$O$_3$: the former TLSs show sudden switchings in energy or even become invisible in time within the resonator bandwidth, making it more difficult to identify individual TLSs. This leads to a higher error in the Monte Carlo fit. We also observed energy features that are almost independent of E_{ex}, as indicated by black arrows. They are not expected because all coupled TLSs should be frequency tunable in the device. At -8 kV/m, one hyperbola seems to change slope (as indicated by the start of a blue dashed line), although instead this event may represent a transition in observing two separate TLSs.

Surprisingly, one of them seems to be only partially described by a hyperbola (red-dashed curve). Increasing the bias voltage at -30 kV/m, this TLS seems to switch from a regular TLS state to an unknown state which has constant transition energy under bias until -19 kV/m, and finally switch back to normal TLS behavior. This indicates
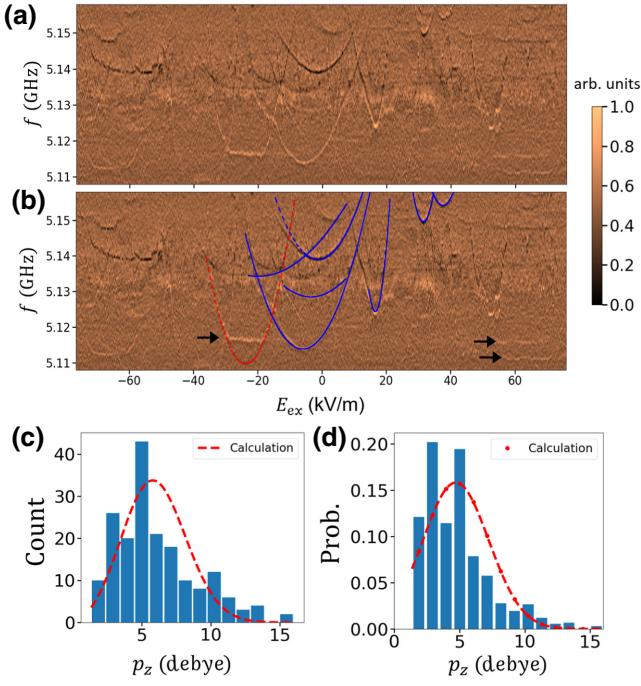
FIG. 3.   (a) Example of processed transmission data on amorphous a-AlO$_x$ film resonator versus frequency f and external electric field E_{ex} (see main text). The *LC* resonance is approximately 5.132 GHz (no longer visible after data processing). (b) The same data with lines fitted to the TLS energy function. Seven fitted dipole moments are extracted at values of 3.2–12.7 D. TLSs whose energy does not depend on bias voltage are marked by arrows. A curved red dashed line shows an anomalous TLS; it switches between a hyperbola and a nearly constant energy of 5.116 GHz at $E_{ex} = -30$ kV/m and $E_{ex} = -18$ kV/m. (c) The measured distribution of 189 TLSs and a Seaborn box. The green line represents the largest dipole measured in γ-Al$_2$O$_3$. (d) The probability of the material TLS dipole distribution. Dashed lines in (c) and (d) are modified and regular Gaussian functions and obtained by two methods. The red lines are acquired by calculation, and the yellow lines are acquired by fitting. We report a mean dipole of 4.6 ± 0.5 D and $\sigma = 2.5 \pm 0.3$ D. Analysis on missing extracted dipoles was needed in the amorphous film, but it also gives a mean value much larger than in the γ-Al$_2$O$_3$ (see main text and Appendix G).

an unexpected state near its energy minima Δ_0, which we believe has not been identified previously.

Unlike the other sample, the amorphous films show most of the hyperbolas from TLSs in the bias range of -30 to 30 kV/m (more data can be found in [58]). Outside of this range TLSs tracks are seen, but they do not trace out a smooth hyperbola. Furthermore, we find after repeating the voltage scanning within the same cooldown that most TLSs do not appear twice. In a small fraction of TLS hyperbolas (less than 3%) a TLS hyperbola has the same dipole and the minimum in energy is within 1 MHz, such that it is regarded as the same TLS and disregarded in distribution.

In a-Al$_2$O$_3$, we identify and analyze a total of 189 TLSs using multiple field sweeps and cooldowns according to the above procedure. The measured distribution $H(p_z)$ with counts and the probability of material distribution $D(p_z)$ are shown in Fig. 3(c). The extracted p_z shows a broad range in value from 0.5 D to 16 D with an average of 6.0 D and an interquartile range (from the 25th to 75th percentiles) of 3.8 D. Because of the large deviation, we cannot get a reasonable fitting to a Gaussian from the MLE method as shown in yellow lines, which have mean value of 1.6 D and standard deviation of 4.2 D. Instead, we calculate the material average dipole moment $\bar{p}_z$ for $D(p_z)$ from $H(p_z)$, using $\bar{p}_z = \int p_z D(p_z) dp_z / \int D(p_z) dp_z = \int H(p_z) dp_z / \int p_z^{-1} H(p_z) dp_z$, and the standard deviation in a similar way. From this we find $\bar{p}_z = 4.6 \pm 0.5$ D $(= 0.96 \pm 0.1\, e\,\text{Å})$ and $\sigma = 2.5 \pm 0.3$ D $(= 0.52 \pm 0.05\, e\,\text{Å})$. A Gaussian curve with these parameters is plotted as a red dashed line.

The calculated loss from the dipole distribution is 3.2×10^{-4} which is smaller than the 9.75×10^{-4} reported above. The missing TLS extraction happens in two ways. On the one hand, larger p_z TLSs have a higher possibility of interacting with other TLSs and their frequencies are prone to switch to other states or diffuse. On the other hand, small p_z TLSs require a longer time to acquire TLS hyperbolas and the signal-to-noise ratio is smaller due to smaller coupling to the resonator. As a result, the TLS extraction does not include most of the TLS, unlike the extraction in γ-Al$_2$O$_3$. We estimate the minimum mean moment of amorphous alumina from missing TLSs. We make no claim about anisotropy in this film since the missing TLSs may create one of the peaks in the distribution of p_z (Appendix G).

To decipher the role of TLS–TLS interaction, we next conduct temporal spectroscopies for the two different film types: γ-Al$_2$O$_3$ and a-AlO$_x$. Figure 4 shows processed S_{21} traces observed over many hours. This resonant TLS noise is believed to be caused by interactions with thermally excited low-frequency TLSs [13,59]. As shown in Fig. 4(a), TLSs biased at 0 V in γ-Al$_2$O$_3$ films near the resonance frequency are relatively stable: their energies drift by less than 2 MHz over tens of hours. In contrast, TLSs in a-AlO$_x$ behave similarly to Ref. [13]. TLSs show irregular drifts of more than 5 MHz, including multiple telegraphic switching events (blue arrows) and abrupt TLS shifts (black arrow). Due to the larger dipole moments observed in a-AlO$_x$, we expect a larger interaction than that in γ-Al$_2$O$_3$ (assuming that the low-frequency thermally activated TLSs are similar to the high-frequency ones). The large unstable behaviors shown in the amorphous films occur in a few hours; for example, a 4 D hyperbola track in a-AlO$_x$ data took about 5 h to obtain.

Comparable results on amorphous alumina exist. One study found p_z in the range of 2.3–7.4 D, using a few
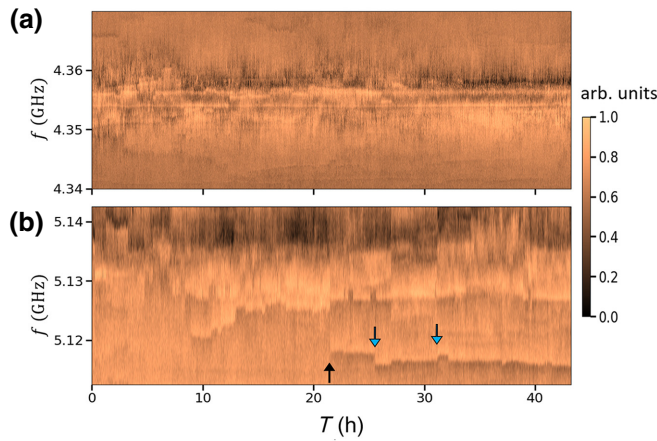
FIG. 4. Time dependence of processed $|S_{21}|$ with a frequency range of at least 30 MHz. (a) γ-Al$_2$O$_3$ spectroscopy shows the TLSs are relatively stable in frequency near the transmission minimum for tens of hours. (b) a-AlO$_x$ spectroscopy shows relatively large TLS energy switching and drift.

analyzed TLSs [40]. Other field-tuned measurements in a-AlO$_x$, studying the barrier of JJs, detected several moments with p_z between 1.0 D and 2.9 D [35]. Measurements of the transition dipole moments in a-AlO$_x$ of JJs indicate that $p_z \leq 6.0$ D [8] and $p_z \leq 4.8$ D [60] in two TLS dipoles measured. The existing data on amorphous alumina TLSs seems consistent with our observations, though the growth methods are slightly different.

Finally, we return to comment on the possible origins of TLSs in our alumina from a comparison to recent TLS DFT [47–50] and molecular dynamics [51] simulations on aluminum oxide. Two models related to hydrogen suggest total dipole moment $p < 3.0$ D [47,48]. Holder *et al.* find that hydrogen aluminum-vacancy TLSs $V_{Al} - H$ in α-Al$_2$O$_3$ have $p = 3.0$ D [47]. Separately, Gordon *et al.* simulated the interstitial hydrogen in α-Al$_2$O$_3$ at various two-oxygen-atom distances where p lay in the range 2.2–2.7 D [48]. Besides H-based simulations, two models of O-based TLSs suggest $p > 4.2$ D. DuBois *et al.* studied models of delocalized oxygen atoms with six neighboring aluminum atoms [49,50]. They found oxygen-deficient AlO$_x$ for $x = 1.25$ by varying distances between O and Al atoms, with p between 4.2 D and 6.5 D for TLSs with tunneling energy $\Delta_0/h = 4$ GHz [49]. Additionally, Paz *et al.* found natural bistable structures in amorphous alumina including only Al and O atoms and calculate an average $p = 4.2$ D from seven TLSs [51]. Although there are difference between theoretical models, they are consistent in that hydrogen TLSs have smaller p than oxygen TLSs.

The γ-Al$_2$O$_3$ $D(p_z)$ has a single peak at approximately $p_z = 2.6$ D, which can be sourced from hydrogen TLSs or two unresolved peaks of both hydrogen and oxygen TLSs. Although small statistically, a-AlO$_x$ has a wider

spread in $D(p_z)$ and two separate peaks. Furthermore, a-AlO$_x$ TLSs have 10% population with $p_z > 8.6$ D, where $p_z = 8.6$ D is the maximum in γ-Al$_2$O$_3$. Using a comparison between two alumina datasets and the fact that O-based TLS is the larger dipole in DFT structures, we find a higher ratio of oxygen TLSs to hydrogen TLSs in a-AlO$_x$ than in γ-Al$_2$O$_3$.

IV. CONCLUSION

In summary, we have extracted the dipole moment p_z of hundreds of individual TLSs in nanoscale-thick films of (polycrystalline) γ-Al$_2$O$_3$ and (amorphous) a-AlO$_x$ alumina. We have used an electrical-bridge quantum-defect sensor, which we show is suitable for characterizing a large number of TLSs as quantum defects. Analysis of the measured histogram of p_z reveals that polycrystalline alumina fits well to a single Gaussian peak. From the material distribution (algebraically related to the measured one), we obtain that the mean TLS moment of the polycrystalline film is $p_z = 2.6 \pm 0.3$ D ($= 0.54 \pm 0.05\, e\,\text{Å}$) with $\sigma = 1.6 \pm 0.2$ D ($= 0.33 \pm 0.03\, e\,\text{Å}$). Furthermore, the material distribution disagrees with the isotropic model commonly used in amorphous materials, indicative of a preferred texture (orientation) of the polycrystalline grains which host TLSs. On the other hand, we cannot conclude if amorphous alumina dipoles are isotropic or not because of missing TLS data extractions.

The accurate mean p_z puts constraints on its defect type, and allows us to make an initial comparisons to microscopic structures used in DFT calculations. The polycrystalline data show one dominant peak, and could be showing dominance of hydrogen TLSs, or unresolved peaks of both hydrogen and oxygen TLSs in the distribution. We find that a-AlO$_x$ has a larger mean $p_z = 4.6 \pm 0.5$ D, which is consistent with previous amorphous alumina results. In contrast to γ-Al$_2$O$_3$, the TLSs switch more rapidly, and our p_z distribution in amorphous alumina yields a larger standard deviation ($= 2.5 \pm 0.3$ D) and two peaks in contrast to one. The moments above 8.6 D (10% of the distribution) are larger than any TLS in polycrystalline alumina and agree only with calculations of delocalized O atoms. Due to this and other amorphous distribution features, we find that the ratio of oxygen to hydrogen TLSs is higher in amorphous samples than in the polycrystalline ones. Because a simple distribution is found in one case, alumina seems to be an important material for further JJ barrier studies.

APPENDIX A: MATERIAL DENSITY AND LOSS TANGENT

In this appendix we derive the relationship between material TLS density, $D(p_z)$, and the measured histogram, $H(p_z)$. In the Standard Tunneling Model [41,42], the authors assume that the density of levels per unit volume and energy, $n(\Delta, \Delta_0)$, depends on tunneling energy Δ_0 but is uniform in Δ, giving

$$n(\Delta, \Delta_0)\, d\Delta d\Delta_0 = \frac{P_0}{\Delta_0}\, d\Delta d\Delta_0, \qquad (A1)$$

where P_0 is a constant in units of $J^{-1}\, m^{-3}$. However, the model only considers a single moment $|\vec{p}| = p$. In our experiments, we notice the dipole moment on the z axis is not uniform and we add dipole direction and magnitude dependence. For the general case, we write

$$n(\Delta, \Delta_0, \vec{p})\, d\Delta d\Delta_0 d^3 p = \frac{P_0'}{\Delta_0} D(\vec{p})\, d\Delta d\Delta_0 d^3 p, \quad (A2)$$

where $D(\vec{p})$ is a generalized material TLS distribution and P_0' is a new constant. However, $D(\vec{p})$ depends on three Cartesian coordinates, and we only have measurement access to one component, p_z. A full investigation of $D(\vec{p})$ is beyond the scope of this paper, but we assume that $D(\vec{p})$ is separable in p_x, p_y, and p_z. Therefore, we consider the case

$$n(\Delta, \Delta_0, p_z) d\Delta d\Delta_0 dp_z = \frac{D(p_z)}{\Delta_0}\, d\Delta d\Delta_0 dp_z, \quad (A3)$$

where $\int D(p_z)\, dp_z = P_0$ and $D(p_z)$ is the material density mentioned in the main text. In TLS spectroscopy, V_{bias} is controlled such that p_z, Δ_0, and $\Delta|_{V_{\text{bias}}=0}$ can be extracted for individual TLSs and $\Delta = \Delta|_{V_{\text{bias}}=0} + 2p_z V_{\text{bias}}/l_0$, where l_0 is the thickness of dielectric. Next, we change variables to include V_{bias} through Jacobian transformation, giving

$$d\Delta dp_z = dp_z dV_{\text{bias}} \begin{vmatrix} \frac{\partial \Delta}{\partial p_z} & \frac{\partial \Delta}{\partial V_{\text{bias}}} \\ \frac{\partial p_z}{\partial p_z} & \frac{\partial p_z}{\partial V_{\text{bias}}} \end{vmatrix} = \left(\frac{2p_z}{l_0}\right) dp_z dV_{\text{bias}}. \quad (A4)$$

N_{tot} is the total number of observed TLSs from the measurement histogram, $H(p_{zi})$,

$$N_{\text{tot}} = \sum_i H(p_{zi}) \Delta p_{zi}, \qquad (A5)$$

where p_{zi} is the center value and Δp_{zi} is the bin width of the ith bin. Related to Eq. (A3), N_{tot} can also be written as

$$N_{\text{tot}} = \mathbb{V} \int n(\Delta, \Delta_0, p_z) d\Delta d\Delta_0 dp_z. \qquad (A6)$$

Substituting Eq. (A4) into the above equation, we have

$$N_{\text{tot}} = \mathbb{V} \int_{p_{\min}}^{p_{\max}} D(p_z) \cdot \left(\frac{2p_z}{l_0}\right) dp_z \int_{V_1}^{V_2} dV_{\text{bias}} \int \frac{d\Delta_0}{\Delta_0}. \quad (A7)$$

Similarly, we consider the ith bin of $H(p_{zi})$ and the number of TLSs in this bin,

$$N_i = H(p_{zi}) \Delta p_{zi}. \qquad (A8)$$

In the case of small enough Δp_{zi} and Δ_0, we obtain

$$H(p_{zi}) \Delta p_{zi} = \mathbb{V} \left(\frac{2p_{zi}}{l_0}\right) D(p_{zi}) \Delta p_{zi} \Delta V_{\text{bias}} \frac{\Delta f_0}{f_0} \quad (A9)$$

or

$$D(p_z) = \frac{1}{\mathbb{V}} \frac{H(p_z)}{2p_z} \frac{l_0}{\Delta V_{\text{bias}}} \frac{f_0}{\Delta f_0}, \qquad (A10)$$

where Δf_0 is the measurement frequency span. Thus, we prove that $D(p_z)$ is not proportional to the measured histogram $H(p_z)$, but $D(p_z) \propto H(p_z)/p_z$.

Next, we derive the loss tangent, $\tan \delta_0$, from the TLS histogram. Following Ref. [17], loss due to TLSs can be described as

$$\tan \delta = \int \frac{p_z^2}{\varepsilon} \frac{-\frac{1}{T_2} \tanh\left(\frac{E_{\text{TLS}}}{2k_B T}\right)}{(T_2^{-2} + \Omega^2 \frac{T_1}{T_2}) + \left(\frac{E_{\text{TLS}}}{\hbar} - 2\pi f_0\right)^2} d^3 n$$

$$= \int D(p_z) \frac{p_z^2}{\varepsilon} \frac{-\frac{1}{T_2} \tanh\left(\frac{E_{\text{TLS}}}{2k_B T}\right) d\Delta \frac{d\Delta_0}{\Delta_0}}{(T_2^{-2} + \Omega^2 \frac{T_1}{T_2}) + \left(\frac{E_{\text{TLS}}}{\hbar} - 2\pi f_0\right)^2} dp_z, \quad (A11)$$

where ε is the permittivity constant, Ω is the Rabi frequency, and T_1 (T_2) is TLS relaxation (decoherence) time. The derivation of a similar integral has been presented in Ref. [17]. In the case when $\Omega^2 T_1 T_2$ is much smaller than 1,

$$\tan \delta = \frac{\pi}{\varepsilon} \int D(p_z) p_z^2 dp_z. \qquad (A12)$$

Next, we estimate the loss tangent of γ-Al_2O_3. By substituting $D(p_z)$ from Eq. (A10), we get

$$\begin{aligned} \tan \delta &= \frac{\pi}{\varepsilon} \frac{1}{\mathbb{V}} \int \frac{H(p_z)}{2p_z} \frac{l_0}{\Delta V_{\text{bias}}} \frac{f_0}{\Delta f_0} p_z^2\, dp_z \\ &= \frac{\pi}{2\varepsilon} \frac{l_0}{\mathbb{V} \Delta V_{\text{bias}}} \frac{f_0}{\Delta f_0} \int H(p_z) p_z dp_z \\ &\approx \frac{\pi}{2\varepsilon} \frac{l_0}{\mathbb{V} \Delta V_{\text{bias}}} \frac{f_0}{\Delta f_0} \sum H(p_z) p_z \Delta p_z \\ &= \frac{\pi}{2\varepsilon} \frac{l_0}{\mathbb{V} \Delta V_{\text{bias}}} \frac{f_0}{\Delta f_0} \sum_i^{394} p_{zi} = 1.4(1) \times 10^{-3}. \end{aligned} \quad (A13)$$

The function is factor of π larger than that in Eq. (S6) in Ref. [34]. Notice that the loss tangent from the TLS histogram is similar to the bulk resonator loss tangent, $\tan \delta_0 = 1.5 \times 10^{-3}$, reported in main text. Finally, we estimate the material constant in the same film,

$$
\begin{aligned}
P_0 &= \int D(p_z) dp_z \\
&\approx \sum_i \frac{1}{\mathbb{V}} \frac{1}{p_{zi}} \frac{l_0}{2\Delta V_{\text{bias}}} \frac{f_0}{\Delta f_0} = 1.0(1) \times 10^{44} \ (\text{J}^{-1}\text{m}^{-3}).
\end{aligned}
$$

$$(A14)$$

In contrast to γ-Al$_2$O$_3$, the loss tangent of amorphous alumina is $3.2(3) \times 10^{-4}$ which is a few times smaller than the measured amorphous alumina loss tangent $[= 9.8(9) \times 10^{-4}]$. This is expected because we do not fit those TLSs with uncompleted hyperbola curves.

APPENDIX B: INTERNAL QUALITY FACTOR FITTING AND BIAS FILTERING

In this appendix we discuss the effect of bias line filtering and TLS noise on resonator data fittings. Filtering noise in the bias line is essential to study the individual TLSs in both film types. We performed a controlled experiment with additional bias-line noise. We start from a setup where the bias line has only a low-pass copper powder filter and a 12 GHz K&L Microwave brand filter. Figure 5(a) shows measurements of γ-Al$_2$O$_3$ TLS spectroscopy with low-frequency noise and Fig. 5(b) shows one $|S_{21}|$ at fixed bias. There is no observation of any individual TLS. Surprisingly, the fit gives an internal quality factor, $Q_{i,\text{noise}} = 1600$, which is higher than the $Q_i = 680$ reported in the main text. It is believed that without proper noise filtering, the bias voltage noise strongly affects the visibility of the TLSs. The change of TLS frequency due to voltage noise is

$$
\delta \omega_{\text{TLS}} = \frac{\Delta}{\hbar E_{\text{TLS}}} \delta \Delta = \frac{\Delta}{\hbar E_{\text{TLS}}} \times 2 p_z \delta V_{\text{ex}} / l_0. \qquad (B1)
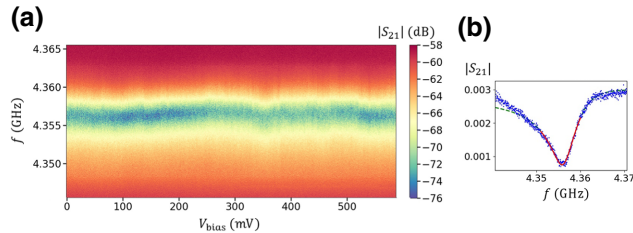$$

(a)

(b)

FIG. 5. (a) Spectroscopy of dc bias sweep on γ-Al$_2$O$_3$ with voltage noise. (b) One example of $|S_{21}|$ from (a) without proper filtering. Voltage noise obscures TLSs within the spectrum and $Q_i = 1600$.

In the case of multiple TLSs coupled to a resonator, the transmission rate is given by [61]

$$
S_{21}(\omega) = 1 - \frac{\kappa_c/2}{\frac{\kappa_c + \gamma_c}{2} + i(\omega - \omega_c) + \sum \frac{g_i^2}{\gamma_i/2 + i(\omega - \omega_i)}},
$$

$$(B2)$$

where κ_c is the cavity's decay rate to the transmission line, γ_c is the cavity decay rate to the environment when no TLSs exist, ω_c is the cavity resonance, g_i is the coupling strength of each TLS, γ_i is the decoherence rate, and ω_i is the resonant frequency of the ith TLS. Inspired by Ref. [62], we assume that every TLS experiences a Gaussian voltage noise and we rewrite transmission rate as

$$
S_{21} = 1 - \frac{\kappa_c}{2} \int \cdots \int \frac{\prod_i \sqrt{\frac{1}{2\pi\sigma_i}} \exp\left[\frac{-\delta\omega_i^2}{2\sigma_i}\right] d\delta\omega_i \cdots d\delta\omega_n}{\frac{\kappa_c + \gamma_c}{2} + i\Delta_c + \sum \frac{g_i^2}{\frac{\gamma_i}{2} + i(\Delta_i + \delta\omega_i)}},
$$

$$(B3)$$

where $\Delta_c = \omega - \omega_c$ and $\Delta_i = \omega - \omega_i yy$ The standard deviation, σ_i, of the ith TLS depends on δV_{ex} and p_z such that the sensitivity to voltage noise is described as an averaged effect. The enhancement of σ_i eliminates the effect of the ith TLS. A simulation of different σ_i is shown in Fig. 6(a). Two TLSs are coupled to the resonator. The upper TLS in the plot is not affected by voltage noise and the lower TLS in the plot has g, γ_0, and a random frequency shift with deviation, σ. Simulations show that the lower TLS has smaller and smaller effect on the resonator, while voltage noise (or σ) increases. The phenomenon of the voltage noise is qualitatively similar to the increasing decoherence γ of TLS as shown in Fig. 6(b).

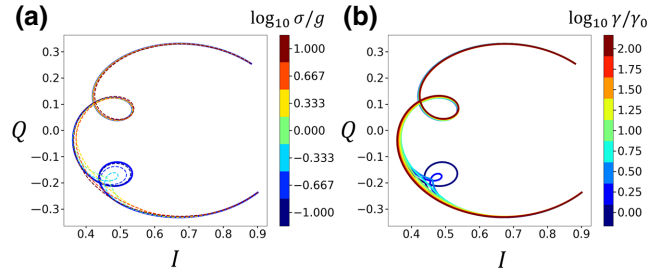**(a)** $\log_{10} \sigma/g$ **(b)** $\log_{10} \gamma/\gamma_0$

FIG. 6. Simulation of Eq. (B3) with resonator parameters $\kappa_c, \gamma_c = 4$ MHz, $f_c = 4$ GHz, and two TLSs having $g = 0.7$ MHz, $\gamma_0 = 0.5$ MHz. Only one of them is affected by voltage noise (the lower one). (a) The solid blue line shows resonator coupled to two TLSs and both have no voltage noise. The colored dashed lines show the enhancement of σ from $0.1 \times g$ to $10 \times g$ on the lower TLS. (b) Simulation of the lower TLS under enhanced decoherence rate. The colored lines indicate the behavior of the lower TLS is similar to enhancement of σ in (a).

APPENDIX C: FITTING OF THE AVERAGED S_{21} OF a-AlO$_x$

Due to the low Q (below 250) in the a-AlO$_x$ resonator, the resonator's transmission data are easily perturbed by frequency-dependent background. For example, there will be: (1) spurious modes existing in the input-output cables, the sample box or on the chip; and (2) electrical components such as amplifiers, circulators, or attenuators. One obvious result is that the off-resonant part of the I–Q plot deviates from the circle-fitting curve where $|S_{21}|$ is not constant. Thus, we modified the fitting function to better extract the resonator's parameters. We consider the background as multiple low-Q modes, which have no direct coupling with each other and our resonator and the their transmission rate

$$S_{21,\text{low}Q} = \prod_{k=1}^{N} \left(1 - \frac{Q_k/Q_{e,k}}{1 - 2\,i\,Q_k\,(\omega - \omega_k)/\omega_k} \right), \quad (C1)$$

where $Q_k, Q_{e,k}$, and ω_k are the total quality factor, external quality factor, and resonant frequency, respectively. In general, in a small range around resonant frequency ω_0, the background can be simplified to $[1 + (a + ib)(\omega - \omega_0)]$, where a and b are constant. If the Q of the nearest mode to the measured resonator is of the order of 10 and $Q_e/Q_i \lesssim 1$ and each mode is more than 100 MHz spaced from the next nearest mode, $S_{21,\text{low}Q}$ can be expanded around ω_0 to the first order of ω. As a result, the final fitting function is

$$S_{21} = C[1 + (a + ib)(\omega - \omega_0)]e^{i\theta}\left(1 - \frac{Q/Q_e e^{i\phi}}{1 + 2i\frac{Q}{\omega_0}(\omega - \omega_0)} \right). \quad (C2)$$

Figure 7 shows two averaged S_{21}, which are normalized to 1, from two different cooldowns: (a) and (b) are from the dataset of Fig. 8; (c) and (d) are from the dataset shown in the Supplemental Material [58]. To our surprise, the Q_i of the a-AlO$_x$ sample are distinct in different cooldowns and the fits vary from 710 to 1510. We do not understand this variance in amorphous sample and no significant Q_i changes for our γ-Al$_2$O$_3$ sample in different cooldowns.

The new averaged of Q_i is 1020 for amorphous alumina, which is 1.5 times higher than γ-Al$_2$O$_3$. However, the loss tangent is lower in amorphous alumina probably for two reasons. First, amorphous alumina can have smaller density of TLSs with higher average dipole moment and lower loss tangent in the end. Second, amorphous alumina has

(a)

$Q = 156$
$1/\text{Re}[1/Q_e] = 200$
$Q_e = 170$
$Q_i = 710$
$f_c = 5.142$
$\phi = 329$ °

(c)

$Q = 206$
$1/\text{Re}[1/Q_e] = 257$
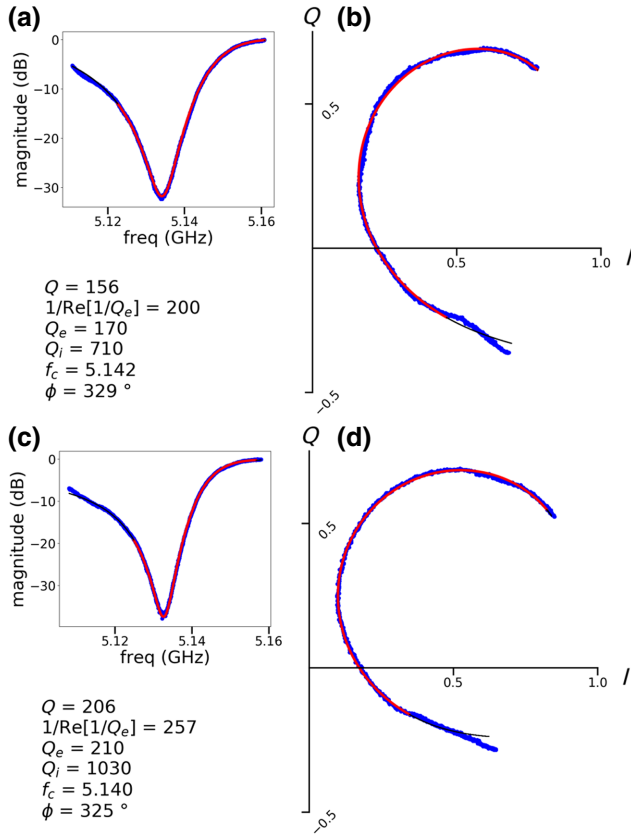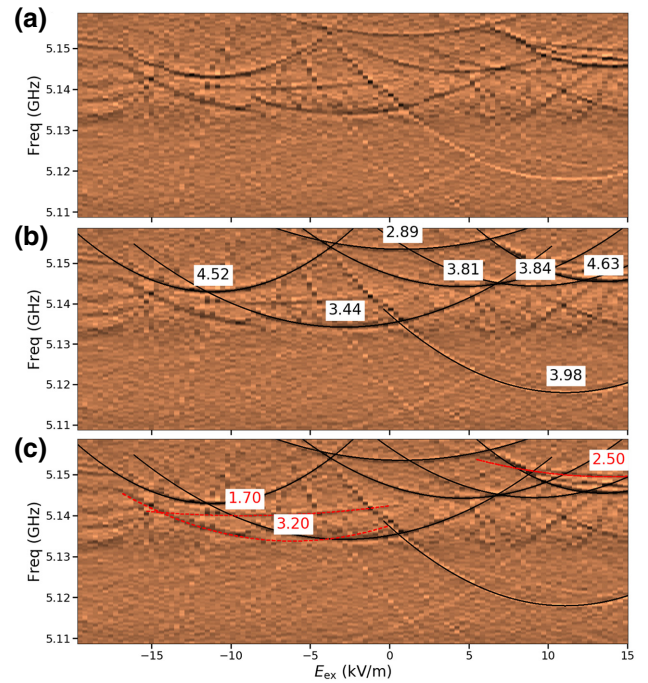$Q_e = 210$
$Q_i = 1030$
$f_c = 5.140$
$\phi = 325$ °

FIG. 7. The normalized $S_{21,\text{avg}}$ of TLS spectrum of a-AlO$_x$, which is similar to the black line in Fig. 1(b). Unlike Fig. 1(b) in the main text, we add a frequency dependent on I and Q for a better fit. The red line represents the fitting range and the black line is the extension of fit to the measurement frequency range. (a),(b) The fitting result shows $Q_i = 710$ and the dataset is from Fig. 8. (c),(d) The dataset is shown in the Supplemental Material. The fitting result shows $Q_i = 1030$.

FIG. 8. One TLS spectroscopy of a-AlO$_x$ TLS. (a) Original data. (b) TLS fitting results and their dipole p_z (D). (c) TLSs with incomplete hyperbolas in red and their potential p_z (D).

higher voltage noise which eventually reduces the coherent time of TLS and loss tangent. Due to the smaller film thickness and a larger portion of large dipole TLS in a-AlO_x, TLSs in a-AlO_x suffer from larger voltage noise than those in γ-Al_2O_3. One example of extreme cases of high voltage noise is shown in Fig. S1 in the Supplemental Material, where we see no TLS and $Q_i = 1600$ is larger than $Q_i = 680$ reported in the main text.

APPENDIX D: FITTING OF HYPERBOLAS IN DC SWEEP PLOT

This appendix describes the procedure of fitting the TLS dipole for Figs. 2 and 3 in the main text. We search the local minimum (hybridized state) of each $|S_{21}|$ from Fig. 2(a) and apply a Gaussian filter on the two-dimensional plot of the local minimum [see Fig. 9(a)]. We obtain the initial guess values of Δ_0, V_{bias}, and p_z for all possible TLS candidates. Due to the complexity of the TLS spectrum, TLSs are fitted separately in the order of their Δ_0 from largest to smallest. The first candidate TLS with the largest Δ_0 is fitted by Monte Carlo method and the result is shown in Fig. 9(b). We assign those local minima to the first TLS and subtract them from Fig. 9(a) to get Fig. 9(c). For the next TLS, we use the local minimum plot from Fig. 9(c) and the next fitting will not be affected by the previous TLS result. We repeat the process until all TLSs are
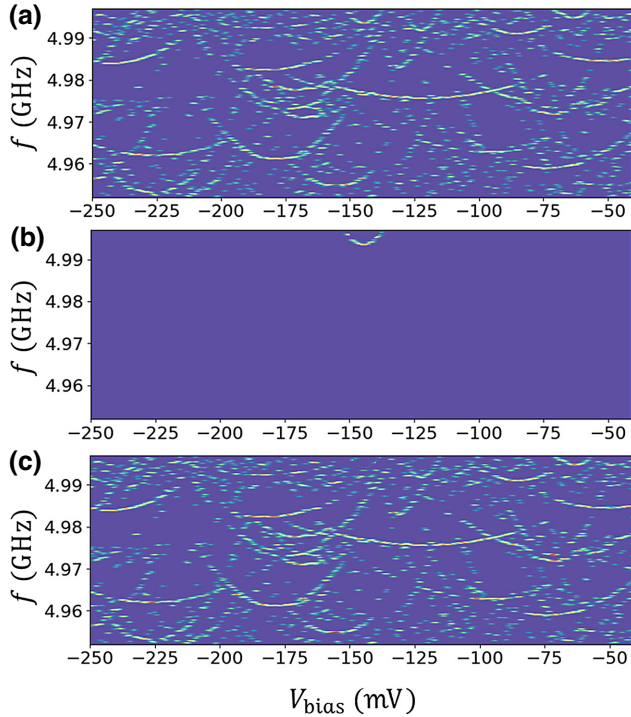

FIG. 9. (a) Plot of extracted minimum energies in Fig. 2 of main text. (b) The final result of the first dipole fit. (c) Subtracting the first dipole fitting result from (a).
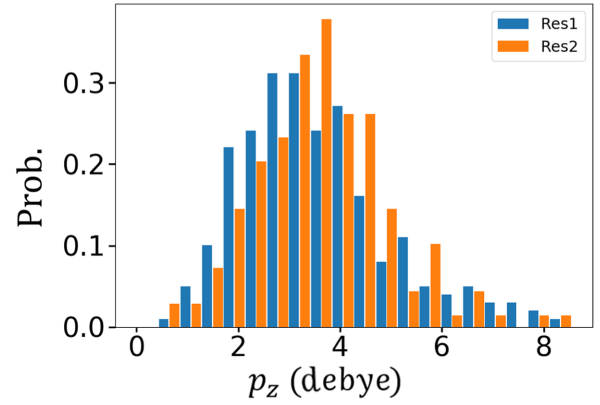

FIG. 10. Histograms of dipole moments from two different γ-Al_2O_3 resonators.

fitted and discard those TLSs not crossing their minimum energies.

APPENDIX E: γ-Al_2O_3 TLS HISTOGRAMS IN TWO DIFFERENT RESONATORS

Figure 10 and Table I show the dipole moment measured in two γ-Al_2O_3 resonators. The mean p_z are 3.5(1) and 3.6(1), for Res1 with $f_0 = 4.35$ GHz and Res2 with $f_0 = 4.95$ GHz, respectively. Figure 11 shows the dipoles measured in four different cooldowns versus either Δ_0 or the external field $E_{ex,min}$, where the TLSs meet their minimum energies.

Amorphous materials rearrange their atom positions when their temperature is above glass transition temperature (T_g). The thermal cycle to room temperature (less than or equal to T_g) is likely not enough. There are chances that TLSs are measured twice in two cooldowns. However, we found the p_z of different cooldowns scatter randomly in the plots (see Fig. 11). Theoretically, TLSs do not change their Δ_0 without reaching T_g. However, we cannot tell if the TLSs' Δ_0 and p_z have changed sufficiently to be considered as new TLSs. But from Figs. 11(b) and 11(d), most TLSs (at least approximately 85%) have different Δ_0 and p_z in different cooldowns. Whether the thermal cycle is constructing a new set of TLSs is beyond the scope of this paper.

TABLE I. Mean and standard deviation of extracted TLS p_z for each γ-Al_2O_3 resonator.

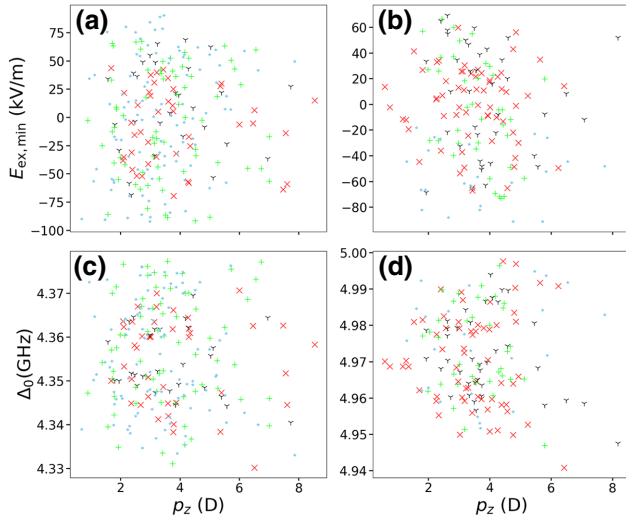|	Mean p_z (D)	Standard deviation (D)
Res1 (4.35 GHz)	3.55	1.47
Res2 (4.95 GHz)	3.64	1.3

FIG. 11. Dipole moments p_z versus Δ_0 or the field of minimum TLS energy $E_{\mathrm{ex,min}}$ in four cooldowns: (a),(b) from the resonator of frequency ≈ 4.35 GHz; (c),(d) from the resonator of frequency ≈ 4.97 GHz. Markers with different colors represent four different cooldowns.

APPENDIX F: FITTING OF TLS DENSITY BY MAXIMUM LIKELIHOOD ESTIMATION

In this appendix we show the procedure of applying Fisher's maximum likelihood estimation on our statistics. For simplicity, we choose a truncated normal distribution as our target function $f(p_z; \mu, \sigma)$ to fit our material density $D(p_z)$, where

$$f(p_z; \mu, \sigma) = C(\mu, \sigma) \frac{1}{\sigma\sqrt{2\pi}} \exp\left(-\frac{(p_z - \mu)^2}{2\sigma^2}\right) \quad \text{(F1)}$$

for $p_z \in [0, \infty)$, in which μ is the mean value, σ is the standard deviation. The normalized constant

$$C(\mu, \sigma) = \frac{2}{1 - \mathrm{erf}(-\mu/\sigma\sqrt{2})} \quad \text{(F2)}$$

depends only on μ and σ, where $\mathrm{erf}(x)$ is error function defined as

$$\mathrm{erf}(x) = \frac{2}{\sqrt{\pi}} \int_0^x \exp(-t^2)dt. \quad \text{(F3)}$$

The likelihood function is given by

$$L = \prod_i f(p_{zi}; \mu, \sigma). \quad \text{(F4)}$$

The necessary conditions for the occurrence of a maximum (or a minimum) are

$$\frac{\partial ln(L)}{\partial \mu} = 0, \quad \frac{\partial ln(L)}{\partial \sigma} = 0. \quad \text{(F5)}$$

As mentioned above in Sec. S-I, $D(p_z)$ is not a directly measurement result, but $H(p_z)$ is. Since there is a weighing factor p_z transferring $D(p_z)$ to $H(p_z)$, we have

$$H(p_z; \mu, \sigma) = N_{\mathrm{tot}} C_1(\mu, \sigma) p_z \exp\left(-\frac{(p_z - \mu)^2}{2\sigma^2}\right). \quad \text{(F6)}$$

A new normalization constant is

$$C_1(\mu, \sigma) = \sigma^2 \exp\left(-\frac{\mu^2}{2\sigma^2}\right) + \mu\sigma\sqrt{\frac{\pi}{2}}\left[1 - \mathrm{erf}\left(-\frac{\mu}{\sigma\sqrt{2}}\right)\right], \quad \text{(F7)}$$

and N_{tot} is the total observed TLS.

We also apply a gamma distribution function,

$$f(x, \alpha, \beta) = \frac{x^\alpha e^{-\beta x}}{\Gamma(\alpha)\beta^\alpha}, \quad \text{(F8)}$$

to fit the data, where $\Gamma(\alpha)$ is a gamma function. The resulting fit gives $\alpha = 5.15$ and $\beta = 1.72$ and mean $= 2.99$ D. However, we expect there is a positive distribution when the dipole equals 0, so that the gamma distribution is not suitable.

The MLE method applied to the amorphous alumina measured histogram does not give the main peak feature adequately in the material distribution $D(p_z)$. Thus, we do not use MLE to report averaged dipole in the amorphous data, but rather a calculated mean and standard deviation. The calculation method is described in the main text.
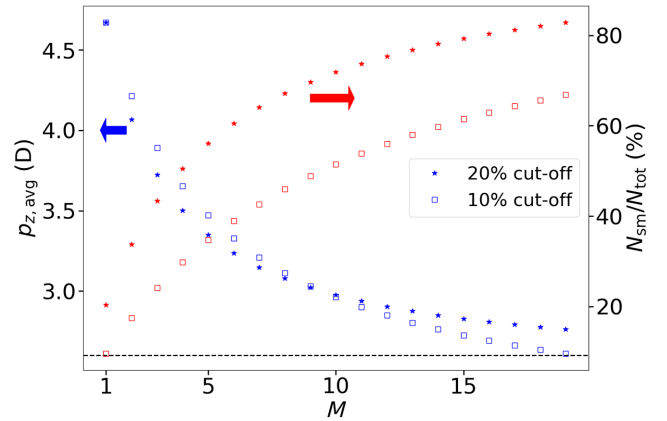

FIG. 12. Computed average dipole for different conditions of plausible missing TLSs in the amorphous film. We take the 10th (2.8 D) or 20th (3.5 D) percentile of p_z in the original data as the maximum value of a "small p_z" set, and make data extrapolations using the adjusted number of small p_z's, as shown in square or star symbols, respectively. Small p_z TLSs in the distribution are multiplied by the multiplication factor M to simulate possible missing TLSs. The original data are when $M = 1$. The black dashed line represents the average dipole in γ-Al$_2$O$_3$. We take $M = 5$ as the most likely case for our data, implying $p_{z,\mathrm{avg}} > 3.3$ D in amorphous alumina film. N_{sm}, number of small dipoles.
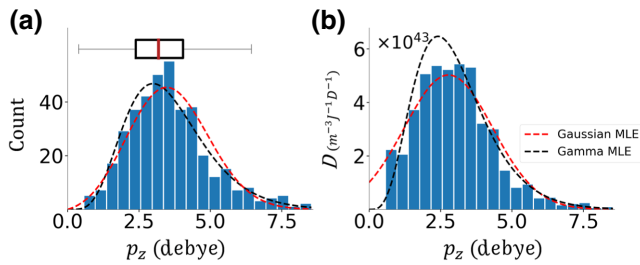
FIG. 13. Gamma distribution MLE analysis on γ-Al$_2$O$_3$ data added to Figs. 2(c) and 2(d) in the main text. (a) Measured distribution. (b) Material distribution. The black dashed lines use the target function of Eq. (S28) in the Supplemental Material to fit the distribution. The red dashed lines represent the Gaussian function as in the main text. The Gaussian function shows a better agreement to the data than the gamma distribution is not suitable (see fit to Gamma MLE in Fig. 11).

APPENDIX G: ESTIMATION OF AVERAGED DIPOLE IN a-AlO$_x$ UNDER TLS FREQUENCY NOISE

Because of the unstable TLS during voltage bias, and resonator noise level, we are prone to measure the larger dipole moments rather than the smaller ones, especially in the amorphous sample. Those TLSs that do not cross their minimum are not counted in statistics due to the high uncertainty. We show a few examples in Fig. 8(c), where preliminary manual fits are shown as dashed lines. On closer examination, one can see some other potential small-dipole-moment TLSs at the edges of the figure.

Here we estimate a case when we miss $M - 1$ out of M small dipole moments by multiplying the small p_z TLS distribution. First, we define the small p_z TLSs as the 10th or 20th percentile, equal to 2.8 D or 3.5 D, respectively. The dipoles smaller than the above value are multiplied M times in counts for a new distribution. The resulting new average dipole p_z and the ratio of the number of small p_z TLSs to the total number are plotted in Fig. 12. Suppose an extreme case with eight missing TLSs and two fitted TLSs with $p_z < 3.5$ D; then four out of five are missed. This implies a factor M of 5 and the new average is at least 3.3 D. This is still larger than $\bar{p}_z = 2.6$ D in γ-Al$_2$O$_3$.

We now turn to the isotropy of dipole orientation. There are missing TLS extractions, especially of those small p_z TLSs. The portion of small p_z TLSs could be underestimated. As a result, if we add those small p_z back, the material distribution $D(p_z)$ could be monotonic, decreasing as expected in the Standard Tunneling Model. More studies are needed to understand the small-dipole TLSs in the amorphous phase.

[1] Y. Nakamura, Y. A. Pashkin, and J. S. Tsai, Coherent control of macroscopic quantum states in a single-cooper-pair box, Nature **398**, 786 (1999).

[2] A. Wallraff, D. I. Schuster, A. Blais, L. Frunzio, R.-S. Huang, J. Majer, S. Kumar, S. M. Girvin, and R. J. Schoelkopf, Strong coupling of a single photon to a superconducting qubit using circuit quantum electrodynamics, Nature **431**, 162 (2004).

[3] V. E. Manucharyan, J. Koch, L. I. Glazman, and M. H. Devoret, Fluxonium: Single cooper-pair circuit free of charge offsets, Science **326**, 113 (2009).

[4] M. H. Devoretand and R. J. Schoelkopf, Superconducting circuits for quantum information: An outlook, Science **339**, 1169 (2013).

[5] F. Yan, S. Gustavsson, A. Kamal, J. Birenbaum, A. P. Sears, D. Hover, T. J. Gudmundsen, D. Rosenberg, G. Samach, and S. Weber, *et al.*, The flux qubit revisited to enhance coherence and reproducibility, Nat. Commun. **7,** 1 (2016).

[6] F. Arute, K. Arya, R. Babbush, D. Bacon, J. C. Bardin, R. Barends, R. Biswas, S. Boixo, F. G. Brandao, and D. A. Buell, *et al.*, Quantum supremacy using a programmable superconducting processor, Nature **574,** 505 (2019).

[7] R. W. Simmonds, K. Lang, D. A. Hite, S. Nam, D. P. Pappas, and J. M. Martinis, Decoherence in Josephson Phase Qubits from Junction Resonators, Phys. Rev. Lett. **93**, 077003 (2004).

[8] J. M. Martinis, K. B. Cooper, R. McDermott, M. Steffen, M. Ansmann, K. Osborn, K. Cicak, S. Oh, D. P. Pappas, and R. W. Simmonds, *et al.*, Decoherence in Josephson Qubits from Dielectric Loss, Phys. Rev. Lett. **95**, 210503 (2005).

[9] J. Burnett, L. Faoro, I. Wisby, V. Gurtovoi, A. Chernykh, G. Mikhailov, V. Tulin, R. Shaikhaidarov, V. Antonov, and P. Meeson, *et al.*, Evidence for interacting two-level systems from the 1/f noise of a superconducting resonator, Nat. Commun. **5**, 1 (2014).

[10] S. M. Meißner, A. Seiler, J. Lisenfeld, A. V. Ustinov, and G. Weiss, Probing individual tunneling fluctuators with coherently controlled tunneling systems, Phys. Rev. B **97**, 180505 (2018).

[11] J. J. Burnett, A. Bengtsson, M. Scigliuzzo, D. Niepce, M. Kudra, P. Delsing, and J. Bylander, Decoherence benchmarking of superconducting qubits, npj Quantum Inf. **5**, 1 (2019).

[12] C. Müller, J. Lisenfeld, A. Shnirman, and S. Poletto, Interacting two-level defects as sources of fluctuating high-frequency noise in superconducting circuits, Phys. Rev. B **92**, 035442 (2015).

[13] P. Klimov, J. Kelly, Z. Chen, M. Neeley, A. Megrant, B. Burkett, R. Barends, K. Arya, B. Chiaro, and Y. Chen, *et al.*, Fluctuations of Energy-Relaxation Times in Superconducting Qubits, Phys. Rev. Lett. **121**, 090502 (2018).

[14] S. Schlör, J. Lisenfeld, C. Müller, A. Bilmes, A. Schneider, D. P. Pappas, A. V. Ustinov, and M. Weides, Correlating Decoherence in Transmon Qubits: Low Frequency Noise by Single Fluctuators, Phys. Rev. Lett. **123**, 190502 (2019).

[15] E. J. Connors, J. Nelson, H. Qiao, L. F. Edge, and J. M. Nichol, Low-frequency charge noise in si/sige quantum dots, Phys. Rev. B **100**, 165305 (2019).

[16] O. Noroozian, J. Gao, J. Zmuidzinas, H. G. LeDuc, and B. A. Mazin, in *AIP Conference Proceedings*, Vol. 1185 (American Institute of Physics, 2009), p. 148.

[17] J. Gao, *The physics of superconducting microwave resonators*, Ph.D. thesis, school California Institute of Technology (2008).

[18] A. D. O'Connell, M. Ansmann, R. C. Bialczak, M. Hofheinz, N. Katz, E. Lucero, C. McKenney, M. Neeley, H. Wang, and E. M. Weig, *et al.*, Microwave dielectric loss at single photon energies and millikelvin temperatures, Appl. Phys. Lett. **92**, 112903 (2008).

[19] E. H. Lock, P. Xu, T. Kohler, L. Camacho, J. Prestigiacomo, Y. J. Rosen, and K. D. Osborn, Using surface engineering to modulate superconducting coplanar microwave resonator performance, IEEE Trans. Appl. Supercond. **29**, 1 (2019).

[20] J. B. Chang, M. R. Vissers, A. D. Córcoles, M. Sandberg, J. Gao, D. W. Abraham, J. M. Chow, J. M. Gambetta, M. Beth Rothwell, and G. A. Keefe, *et al.*, Improved superconducting qubit coherence using titanium nitride, Appl. Phys. Lett. **103**, 012602 (2013).

[21] J. Goetz, F. Deppe, M. Haeberlein, F. Wulschner, C. W. Zollitsch, S. Meier, M. Fischer, P. Eder, E. Xie, and K. G. Fedorov, *et al.*, Loss mechanisms in superconducting thin film microwave resonators, J. Appl. Phys. **119**, 015304 (2016).

[22] C. Quintana, A. Megrant, Z. Chen, A. Dunsworth, B. Chiaro, R. Barends, B. Campbell, Y. Chen, I.-C. Hoi, and E. Jeffrey, *et al.*, Characterization and reduction of microfabrication-induced decoherence in superconducting quantum circuits, Appl. Phys. Lett. **105**, 062601 (2014).

[23] L. Grünhaupt, U. von Lüpke, D. Gusenkova, S. T. Skacel, N. Maleeva, S. Schlör, A. Bilmes, H. Rotzinger, A. V. Ustinov, and M. Weides, *et al.*, An argon ion beam milling process for native alox layers enabling coherent superconducting contacts, Appl. Phys. Lett. **111**, 072601 (2017).

[24] H. Paik, D. Schuster, L. S. Bishop, G. Kirchmair, G. Catelani, A. Sears, B. Johnson, M. Reagor, L. Frunzio, and L. Glazman, *et al.*, Observation of High Coherence in Josephson Junction Qubits Measured in a Three-Dimensional Circuit qed Architecture, Phys. Rev. Lett. **107**, 240501 (2011).

[25] C. Wang, C. Axline, Y. Y. Gao, T. Brecht, Y. Chu, L. Frunzio, M. Devoret, and R. J. Schoelkopf, Surface participation and dielectric loss in superconducting qubits, Appl. Phys. Lett. **107**, 162601 (2015).

[26] O. Dial, D. T. McClure, S. Poletto, G. Keefe, M. B. Rothwell, J. M. Gambetta, D. W. Abraham, J. M. Chow, and M. Steffen, Bulk and surface loss in superconducting transmon qubits, Supercond. Sci. Technol. **29**, 044001 (2016).

[27] C. Deng, Fast control and decoherence in superconducting quantum circuits, (2015).

[28] D. L. Creedon, Y. Reshitnyk, W. Farr, J. M. Martinis, T. L. Duty, and M. E. Tobar, High q-factor sapphire whispering gallery mode microwave resonator at single photon energies and millikelvin temperatures, Appl. Phys. Lett. **98**, 222903 (2011).

[29] K.-H. Lee, S. Chakram, S. E. Kim, F. Mujid, A. Ray, H. Gao, C. Park, Y. Zhong, D. A. Muller, and D. I. Schuster, *et al.*, Two-dimensional material tunnel barrier for josephson junctions and superconducting qubits, Nano Lett. **19**, 8287 (2019).

[30] J. I.-J. Wang, D. Rodan-Legrain, L. Bretheau, D. L. Campbell, B. Kannan, D. Kim, M. Kjaergaard, P. Krantz, G. O. Samach, and F. Yan, *et al.*, Quantum coherent control of a hybrid superconducting circuit made with graphene-based van der waals heterostructures, (2018), arXiv preprint ArXiv:1809.05215..

[31] Y.-P. Shimand and C. Tahan, Bottom-up superconducting and josephson junction devices inside a group-iv semiconductor, Nat. Commun. **5**, 1 (2014).

[32] S. Oh, K. Cicak, J. S. Kline, M. A. Sillanpää, K. D. Osborn, J. D. Whittaker, R. W. Simmonds, and D. P. Pappas, Elimination of two level fluctuators in superconducting quantum bits by an epitaxial tunnel barrier, Phys. Rev. B **74**, 100502 (2006).

[33] M. P. Weides, J. S. Kline, M. R. Vissers, M. O. Sandberg, D. S. Wisbey, B. R. Johnson, T. A. Ohki, and D. P. Pappas, Coherence in a transmon qubit with epitaxial tunnel junctions, Appl. Phys. Lett. **99**, 262502 (2011).

[34] B. Sarabi, A. N. Ramanayaka, A. L. Burin, F. C. Wellstood, and K. D. Osborn, Projected Dipole Moments of Individual Two-Level Defects Extracted Using Circuit Quantum Electrodynamics, Phys. Rev. Lett. **116**, 167002 (2016).

[35] A. Bilmes, S. Volosheniuk, J. D. Brehm, A. V. Ustinov, and J. Lisenfeld, Quantum sensors for microscopic tunneling systems, npj Quantum Inf. **7**, 1 (2021).

[36] A. Bilmes, A. Megrant, P. Klimov, G. Weiss, J. M. Martinis, A. V. Ustinov, and J. Lisenfeld, Resolving the positions of defects in superconducting quantum bits, Sci. Rep. **10**, 1 (2020).

[37] S. de Graaf, S. Mahashabde, S. Kubatkin, A. Y. Tzalenchuk, and A. Danilov, Quantifying dynamics and interactions of individual spurious low-energy fluctuators in superconducting circuits, Phys. Rev. B **103**, 174103 (2021).

[38] J. Lisenfeld, C. Müller, J. H. Cole, P. Bushev, A. Lukashenko, A. Shnirman, and A. V. Ustinov, Measuring the Temperature Dependence of Individual Two-Level Systems by Direct Coherent Control, Phys. Rev. Lett. **105**, 230504 (2010).

[39] G. J. Grabovskij, T. Peichl, J. Lisenfeld, G. Weiss, and A. V. Ustinov, Strain tuning of individual atomic tunneling systems detected by a superconducting qubit, Science **338**, 232 (2012).

[40] J. D. Brehm, A. Bilmes, G. Weiss, A. V. Ustinov, and J. Lisenfeld, Transmission-line resonators for the study of individual two-level tunneling systems, Appl. Phys. Lett. **111**, 112601 (2017).

[41] P. W. Anderson, B. Halperin, and C. M. Varma, Anomalous low-temperature thermal properties of glasses and spin glasses, Philos. Mag. **25**, 1 (1972).

[42] W. Phillips, Tunneling states in amorphous solids, J. Low Temp. Phys. **7**, 351 (1972).

[43] S. de Graaf, L. Faoro, L. Ioffe, S. Mahashabde, J. Burnett, T. Lindström, S. Kubatkin, A. Danilov, and A. Y. Tzalenchuk, Two-level systems in superconducting quantum devices due to trapped quasiparticles, Sci. Adv. **6**, eabc5055 (2020).

[44] C. C. Yuand H. M. Carruzzo, Two-level systems and the tunneling model: A critical view, (2021), arXiv preprint ArXiv:2101.02787.

[45] M. Khalil, S. Gladchenko, M. Stoutimore, F. Wellstood, A. Burin, and K. Osborn, Landau-zener population control and dipole measurement of a two-level-system bath, Phys. Rev. B **90**, 100201 (2014).

[46] S. Matityahu, H. Schmidt, A. Bilmes, A. Shnirman, G. Weiss, A. V. Ustinov, M. Schechter, and J. Lisenfeld, Dynamical decoupling of quantum two-level systems by coherent multiple landau–zener transitions, npj Quantum Inf. **5**, 1 (2019).

[47] A. M. Holder, K. D. Osborn, C. Lobb, and C. B. Musgrave, Bulk and Surface Tunneling Hydrogen Defects in Alumina, Phys. Rev. Lett. **111**, 065901 (2013).

[48] L. Gordon, H. Abu-Farsakh, A. Janotti, and C. G. Van de Walle, Hydrogen bonds in al 2 o 3 as dissipative two-level systems in superconducting qubits, Sci. Rep. **4**, 1 (2014).

[49] T. C. DuBois, M. C. Per, S. P. Russo, and J. H. Cole, Delocalized Oxygen as the Origin of Two-Level Defects in Josephson Junctions, Phys. Rev. Lett. **110**, 077002 (2013).

[50] T. C. DuBois, S. P. Russo, and J. H. Cole, Atomic delocalization as a microscopic origin of two-level defects in josephson junctions, New J. Phys. **17**, 023017 (2015).

[51] A. P. Paz, I. V. Lebedeva, I. V. Tokatly, and A. Rubio, Identification of structural motifs as tunneling two-level systems in amorphous alumina at low temperatures, Phys. Rev. B **90**, 224202 (2014).

[52] C. G. Van de Walleand J. Neugebauer, Universal alignment of hydrogen levels in semiconductors, insulators and solutions, Nature **423**, 626 (2003).

[53] S. Fritz, L. Radtke, R. Schneider, M. Luysberg, M. Weides, and D. Gerthsen, Structural and nanochemical properties of al o x layers in al/al o x/al-layer systems for josephson junctions, Phys. Rev. Mater. **3**, 114805 (2019).

[54] B. Sarabi, A. N. Ramanayaka, A. L. Burin, F. C. Wellstood, and K. D. Osborn, Cavity quantum electrodynamics using a near-resonance two-level system: Emergence of the glauber state, Appl. Phys. Lett. **106**, 172601 (2015).

[55] M. Stoutimore, M. Khalil, C. Lobb, and K. Osborn, A josephson junction defect spectrometer for measuring two-level systems, Appl. Phys. Lett. **101**, 062602 (2012).

[56] M. Khalil, M. Stoutimore, S. Gladchenko, A. Holder, C. Musgrave, A. Kozen, G. Rubloff, Y. Liu, R. Gordon, and J. Yum, *et al.*, Evidence for hydrogen two-level systems in atomic layer deposition oxides, Appl. Phys. Lett. **103**, 162601 (2013).

[57] D. P. Pappas, M. R. Vissers, D. S. Wisbey, J. S. Kline, and J. Gao, Two level system loss in superconducting microwave resonators, IEEE Trans. Appl. Supercond. **21**, 871 (2011).

[58] See supplemental material at http://link.aps.org/supplemental/10.1103/PhysRevApplied.17.034025 for additional spectroscopic fittings to TLSs.

[59] L. Faoroand and L. B. Ioffe, Internal Loss of Superconducting Resonators Induced by Interacting Two-Level Systems, Phys. Rev. Lett. **109**, 157005 (2012).

[60] Y. Shalibo, Y. Rofe, D. Shwa, F. Zeides, M. Neeley, J. M. Martinis, and N. Katz, Lifetime and Coherence of Two-Level Defects in a Josephson Junction, Phys. Rev. Lett. **105**, 177001 (2010).

[61] B. Sarabi, *Cavity quantum electrodynamics of nanoscale two-level systems*, Ph.D. thesis (2014).

[62] B. Brock, M. Blencowe, and A. Rimberg, Frequency Fluctuations in Tunable and Nonlinear Microwave Cavities, Phys. Rev. Appl. **14**, 054026 (2020).